Materials Advances

ROYAL SOCIETY OF CHEMISTRY

COMMUNICATION

View Article Online
View Journal

Open Access Article. Published on 20 January 2026. Downloaded on 1/20/2026 10:35:29 PM.
This article is licensed under a Creative Commons Attribution-NonCommercial 3.0 Unported Licence.

Check for updates

Cite this: DOI: 10.1039/d5ma01446h

Received 11th December 2025,
Accepted 5th January 2026

DOI: 10.1039/d5ma01446h

rsc.li/materials-advances

Controlled sulfidation of silver: a pathway to Ag_2S for short-term synaptic emulation

Shreepooja Bhat,[a] Namitha Bannur,[a] Nanditha Thayyath Kizhakkeveettil,[a] Rajashekhar Pujar[b] and Gurumurthy Sangam Chandrasekhar *[a]

Neuromorphic computing demands scalable, energy-efficient synaptic devices, yet conventional synthesis routes impose prohibitive cost and complexity barriers. This work presents a transformative strategy for material design in which room-temperature exposure to hydrogen sulfide gas converts thermally deposited silver films into phase-pure monoclinic α-Ag_2S, a superionic conductor well-suited for electrochemical metallization (ECM) switching. Structural characterization confirms complete FCC-to-monoclinic phase transformation within 48 hours. Planar Ag/Ag_2S/Ag memristors fabricated from these films exhibit robust unipolar resistive switching with exceptional reproducibility across 16 devices. Systematic pulse-train studies reveal consistent short-term plasticity (STP) behavior, with volatile retention averaging ∼49 seconds at 100 μA compliance. This synthesis approach eliminates vacuum processing requirements, enabling the scalable production of high-performance α-Ag_2S switching layers. This positions ECM devices as accessible and practical elements for neuromorphic hardware.

1 Introduction

The exponential growth of data-intensive applications has intensified the demand for computing architectures that transcend the von Neumann bottleneck inherent to conventional digital processors. Neuromorphic computing, inspired by the brain's massively parallel and energy-efficient signal processing, has emerged as a promising paradigm shift.[1] Synaptic devices are at the core of neuromorphic systems, enabling in-memory computation and adaptive learning capabilities.[2] Recent demonstrations of memristor-based artificial synapses have achieved femtojoule-scale switching operation, delivering multilevel analog-conductance modulation[3] and highly efficient synaptic behavior. Such features facilitate the hardware implementation of both short-term plasticity (STP) and long-term potentiation (LTP),[4] key attributes of biological learning processes. The choice of switching mechanism determines whether a device can exhibit both STP and LTP. Several competing approaches have been explored. Valence change memory relies on oxygen vacancy migration through dielectric oxides, offering high on/off ratios but suffering from discrete, non-linear resistance switching and high switching energies.[5] Phase-change memory achieves impressive data retention through crystal-to-amorphous transitions, but requires crystallization temperatures exceeding 400 °C, which are incompatible with flexible substrates.[6] Neither approach naturally encodes both STP and LTP in a single device architecture. Among resistive switching (RS) mechanisms, electrochemical metallization (ECM) has distinguished itself through its reversible resistive switching properties. In contrast to Valence Change Mechanism (VCM) and Phase Change Memory (PCM) systems, ECM devices operate through voltage induced formation and dissolution of metallic filaments, achieving precise and gradual analog control of conductance states. In ECM devices, active metal electrodes (such as Ag or Cu) undergo electrochemical oxidation under an applied bias. The resulting reaction drives cation migration through solid electrolytes. Cations are subsequently reduced at inert electrodes. This reduction forms conductive filaments.[5] The geometry and thickness of these filaments are closely correlated with pulse amplitude, width, and repetition frequency, governing the transition between transient and persistent conductance states. This mechanism naturally segregates STP from LTP. Transient filament formation under intermittent stimulation produces a volatile conductance enhancement characteristic of dynamic synaptic behavior.[7]

Metal sulfides have gained prominence as ECM electrolytes. They exhibit superior ionic conductivity ($>10^{-3}$ S cm^{-1}). They support mixed Ag^+/electron transport. Their temporal dynamics resemble those of biological synapses, surpassing the performance of oxide-based counterparts. Transition metal sulfides include α-Ag_2S[3], MoS_2,[8,9] WS_2,[10] SnS_2,[11] and Sb_2S_3.[12]

[a] Manipal Institute of Technology, Manipal Academy of Higher Education, Manipal, India. E-mail: gurumurthy.sc@manipal.edu
[b] Manipal Institute of Applied Physics, Manipal Academy of Higher Education, Manipal, India

Open Access Article. Published on 20 January 2026. Downloaded on 1/20/2026 10:35:29 PM.
This article is licensed under a Creative Commons Attribution-NonCommercial 3.0 Unported Licence.

Sulfur-vacancy-assisted ion migration within these materials supports pulse-dependent synaptic plasticity, while the stimulation frequency governs the transition between volatile and non-volatile memory states. Consequently, sulfide-based ECM devices allow precise tuning of STP/LTP ratios *via* pulse parameters an essential feature for implementing metaplastic learning in neuromorphic architectures.[7]

Beyond stable long-term modulation, the transient or short-term memory (STM) responses of such devices are equally critical for real-time neuromorphic functions. STM, which emulates the short-lived synaptic activity seen in biological systems, reflects recent input history rather than permanent storage.[7] Volatile STM behavior can be harnessed for temporal filtering, noise suppression, and dynamic signal preprocessing, enabling selective response to time-correlated.[13–15] This fading-memory characteristic is particularly beneficial for reservoir computing, spike-based encoding, and adaptive sensory perception, where temporal correlation and nonlinearity improve pattern recognition and learning efficiency.[16] Moreover, STM devices are especially attractive for event-driven sensing, edge-AI, and IoT tasks, as they provide energy-efficient transient memory and on-device data processing without frequent refresh operations, setting them apart from conventional non-volatile.[17,18]

Silver sulfide (α-Ag_2S) presents unique advantages among metal sulfides due to its monoclinic phase stability at ambient temperature (below 450 K), exceptional ionic conductivity (10^{-2} S cm^{-1}), and mechanical ductility contrasting sharply with brittle conventional semiconductors.[19,20] The stoichiometric α-Ag_2S phase provides electronic conductivity approximately 10^6 times lower than the superionic β-phase, enabling controlled resistance modulation essential for stable synaptic operation.[21–23] Despite these advantages, conventional synthesis routes remain challenging: solution-based processes require multi-step precipitation with precise pH control, while vacuum deposition demands high temperatures (>200 °C) that often lead to phase impurities and increase production cost.[20,24–26]

Recent studies have shown that exposing Ag-based films or nanostructures to H_2S gas provides a simple and efficient route for forming Ag_2S under mild conditions. Baghirov *et al.* reported vapor-phase sulfidation of Ag nanowires in PVA matrices to yield AgNW/PVA/Ag_2S nanocomposites,[27] and also demonstrated similar transformations in GO/AgNW composites.[28] These reports established the viability of H_2S-induced sulfidation; however, they primarily addressed morphological and optical modifications rather than resistive switching performance.

In this work, a cost-effective and straightforward technique for synthesizing Ag_2S films by exposing thermally synthesized Ag films to H_2S gas in a closed beaker is presented. The process, which transforms FCC Ag into monoclinic Ag_2S, is notable for its minimal steps and use of inexpensive chemicals. Achieving the formation of Ag_2S films at room temperature remains a significant challenge, underscoring the value of the proposed method. With precise control over the exposure conditions, Ag_2S films were successfully synthesized. This innovative approach enables the subsequent investigation of the behaviour of Ag/Ag_2S/Ag devices, highlighting their potential for neuromorphic applications.

2 Experimental procedure

2.1 Chemicals used

Silver wire with a purity of 99.99% was obtained from Hydro Pneo Vac Technologies, India. Sodium sulfide hydrate in flake form ($Na_2S{\cdot}xH_2O$) was sourced from HiMedia Laboratories Pvt. Ltd, India. Concentrated sulfuric acid (H_2SO_4, 98%) was purchased from M/s Loba Chemie Pvt. Ltd, India. Additionally, Milli-Q water was utilised throughout the experimental procedures.

2.2 Experimental details

Glass substrates were meticulously prepared to ensure surface cleanliness and activation before deposition processes. Initially, the substrates were immersed in a chromic acid solution for 24 hours to remove organic contaminants and enhance surface adhesion properties. They were then thoroughly rinsed with Milli Q water to eliminate residual acid. Subsequent cleaning involved immersion in Labolene solution and rinsing with hot water to remove particulate matter and residual chemicals. Furthermore, they were ultrasonicated sequentially in Milli-Q water, acetone, and isopropyl alcohol to effectively remove impurities and organic residues. Finally, the substrates were dried using hot air to prevent recontamination and maintain a pristine surface suitable for subsequent material deposition and characterisation.

2.3 Deposition of Ag_2S thin film

A thin, 100 nm layer of Ag film was deposited onto a glass substrate using thermal vapour deposition. Subsequently, the deposited film underwent a critical exposure phase to H_2S gas inside a closed beaker. This was carried out within a fume hood environment. The generation of H_2S gas was executed with precision by combining 250 mg of sodium sulphide (Na_2S) with a 1 : 1 (v/v) aqueous sulfuric acid solution (H_2SO_4). The process was repeated every 8 hours to consistently generate H_2S gas in a controlled experimental environment. The substrate was later annealed at 60 °C for 2 hours × 6 to eliminate excess sulphur residue. The film was optimised for varying durations (6, 12, 24, 48, and 72 hours) and quantities of Na_2S (250 mg, 500 mg, 1 g, 1.5 g, and 2 g). The optimal conditions were 48 hours duration and 1.5 g of Na_2S. The schematic diagram of the procedure is shown in Scheme 1.

2.4 Ag_2S-based RRAM device fabrication

Silver electrodes were thermally deposited onto the Ag_2S film through a shadow mask to define a lateral Ag/Ag_2S/Ag device structure. The electrodes were spaced 110 μm apart, with a uniform thickness of 150 nm. This planar configuration enabled in-plane electrical measurements. The device was subsequently evaluated for resistive switching and synaptic behaviour.

 © 2026 The Author(s). Published by the Royal Society of Chemistry

Open Access Article. Published on 20 January 2026. Downloaded on 1/20/2026 10:35:29 PM.
This article is licensed under a Creative Commons Attribution-NonCommercial 3.0 Unported Licence.

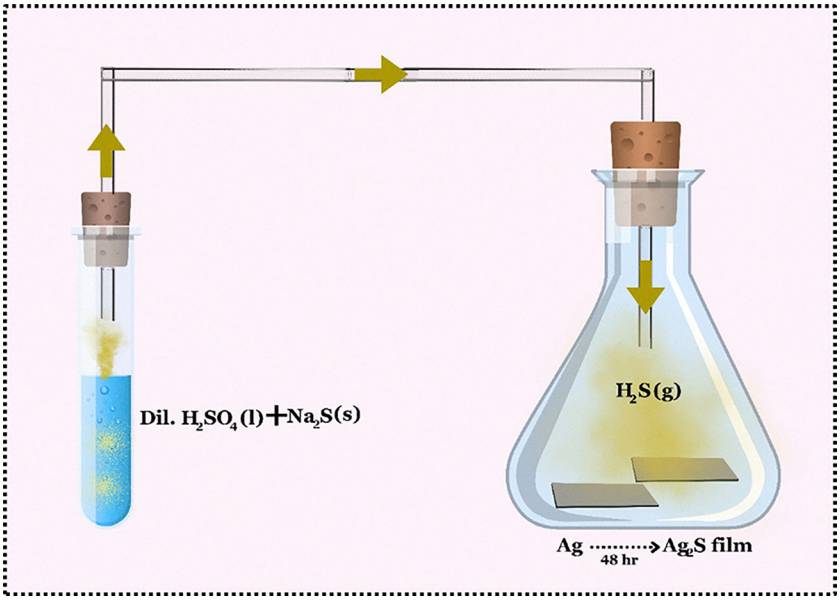

Scheme 1 Schematic diagram illustrating the passage of H_2S gas over the Ag-deposited glass substrate.

3 Results and discussion

3.1 Analysis of structural changes

The interaction between Na_2S and H_2SO_4 results in the formation of H_2S gas, which, when exposed to the Ag film, triggers structural changes that lead to the formation of an Ag_2S layer. The reaction is given in eqn (1) and (2).

$$Na_2S\ (s) + H_2SO_4\ (l) \rightarrow H_2S\ (g) + Na_2SO_4^{-}\ (l) \quad (1)$$

$$Ag\ (s) + H_2S\ (g) \rightarrow Ag_2S\ (s) + H_2^{-}\ (g) \quad (2)$$

Ag in its FCC structure undergoes a transformation to form monoclinic Ag_2S upon exposure to H_2S gas. The process involves a chemical reaction where H_2S gas reacts with the surface of the Ag, causing the S atoms to diffuse into the silver lattice. This diffusion leads to the nucleation and growth of Ag_2S on the Ag-deposited glass substrate. Scheme 2 illustrates the structural transformation of Ag thin film to Ag_2S.

The crystal structure changes from the highly symmetrical FCC lattice of pure Ag to the less symmetrical monoclinic lattice of Ag_2S. In this new structure, Ag atoms occupy different lattice positions than in their original arrangement, resulting in a distinctive monoclinic unit cell characteristic of acanthite, the mineral form of Ag_2S. This structural transformation is driven by the incorporation of S atoms, which disrupts the original metallic bonding in Ag and leads to the formation of ionic bonds characteristic of Ag_2S.

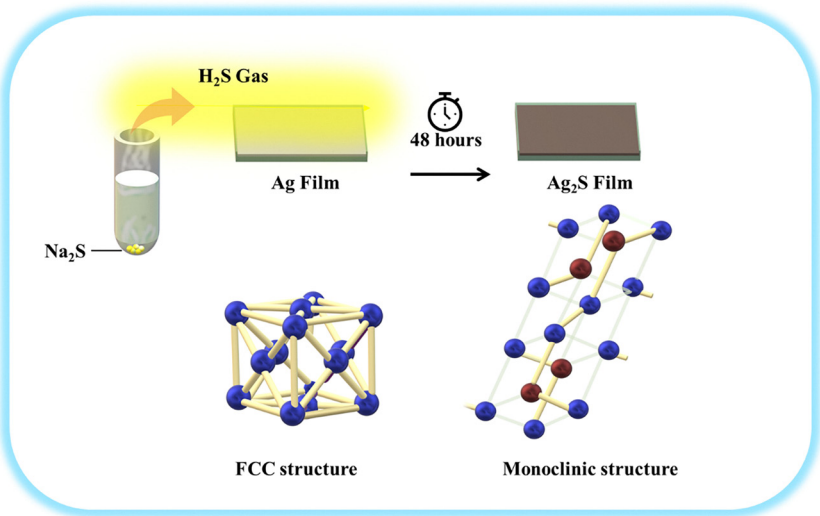

Scheme 2 Schematic representation of the structural changes from Ag to Ag_2S.

Open Access Article. Published on 20 January 2026. Downloaded on 1/20/2026 10:35:29 PM.
This article is licensed under a Creative Commons Attribution-NonCommercial 3.0 Unported Licence.

3.2 Structural and morphological analysis

The XRD patterns of thermally deposited Ag films subjected to sulfurization for durations ranging from 6 to 72 hours are shown in Fig. 1a. The untreated Ag film (AS-00) exhibits distinct diffraction peaks at $2\theta \approx 38.04^\circ$ and 44.20°, corresponding to the (111) and (200) planes of FCC Ag (ICDD 04-0783).[29,30] Upon sulfurization, notable changes in both peak position and phase composition occur as a function of reaction time. In AS-06 and AS-12, the Ag (111) peak shifts to higher angles (38.50° and 38.52°), with the (200) peak also shifting to 44.72° and 44.78°, respectively. These shifts toward higher 2θ values indicate a reduction in interplanar spacing, attributable to compressive strain in the silver lattice.[31] At these initial stages, sulfur species (S^{2-}) do not directly substitute Ag^+ in the lattice. Instead, they may adsorb on the surface or occupy interstitial voids near the surface of the silver lattice. This chemisorption induces localized compressive lattice distortion, as the metallic lattice contracts to accommodate the foreign species.[23,29] Consequently, early sulfurization is governed by surface adsorption and interstitial diffusion mechanisms rather than substitutional lattice replacement.

At 24 and 48 hours (AS-24 and AS-48), the intensity of the Ag peaks diminishes substantially, and new peaks corresponding to monoclinic Ag_2S (ICDD 14-0072) begin to emerge. These include reflections at $2\theta \approx 29.38^\circ$ (021), 31.40° (−112), 33.52° (111), 34.00° (022), 34.60° (022), 36.70° (013), 37.64° (−103), 40.62° (031), and 43.30° (200).[32,33] The appearance and intensification of these Ag_2S peaks confirm the phase transition from metallic Ag to Ag_2S. Some Ag_2S peaks show minor shifts toward lower 2θ angles, indicative of tensile strain introduced by the substitution of larger S^{2-} ions (184 pm) for smaller Ag^+ ions (126 pm), resulting in lattice expansion.[34,35] In contrast, the XRD pattern of the AS-72 sample reveals no discernible diffraction peaks, indicating a complete loss of long-range crystallinity. This suggests that extended sulfurization leads to structural degradation or over-saturation of sulfur, which likely results in film corrosion or the formation of an amorphous phase.[23,29,31,36] Table 1 gives XRD peaks and corresponding planes for AS00-AS72 samples.

SEM analysis revealed S-induced corrosion, highlighting distinct morphological differences between Ag (Fig. 1b) and Ag_2S (Fig. 1c) films. The Ag film exhibited a relatively smooth and continuous surface, indicative of uniform distribution and high film quality.[30,37] In contrast, the Ag_2S film displayed a rougher texture with increased void content, attributed to the incorporation of S atoms. The presence of S within the lattice promoted defect formation and altered the crystal structure, as larger sulfide ions replace smaller Ag ions. This substitution led to lattice expansion, resulting in a more densely packed crystal structure. EDS analysis confirmed the elemental distribution of Ag and S, as shown in Fig. 1e and f, respectively, illustrating the elemental mapping of the Ag_2S film.[29,36,38] These results confirm the transformation of Ag from the FCC phase to the monoclinic phase of Ag_2S after 48 hours of sulfurization. A higher angle shift of Ag and Ag_2S peaks is observed with increasing reaction time, attributed to the transition from FCC Ag monoclinic Ag_2S. This phase transformation is driven by the rearrangement of atoms within the crystal lattice, resulting in a denser monoclinic unit cell and reduced interplanar spacing.[39,40]

3.3 IV characteristics

The *I–V* characteristics of the Ag_2S film were investigated, revealing RS behaviour. The planar Ag/Ag_2S/Ag memristive device, fabricated with an inter electrode spacing of 110 μm,

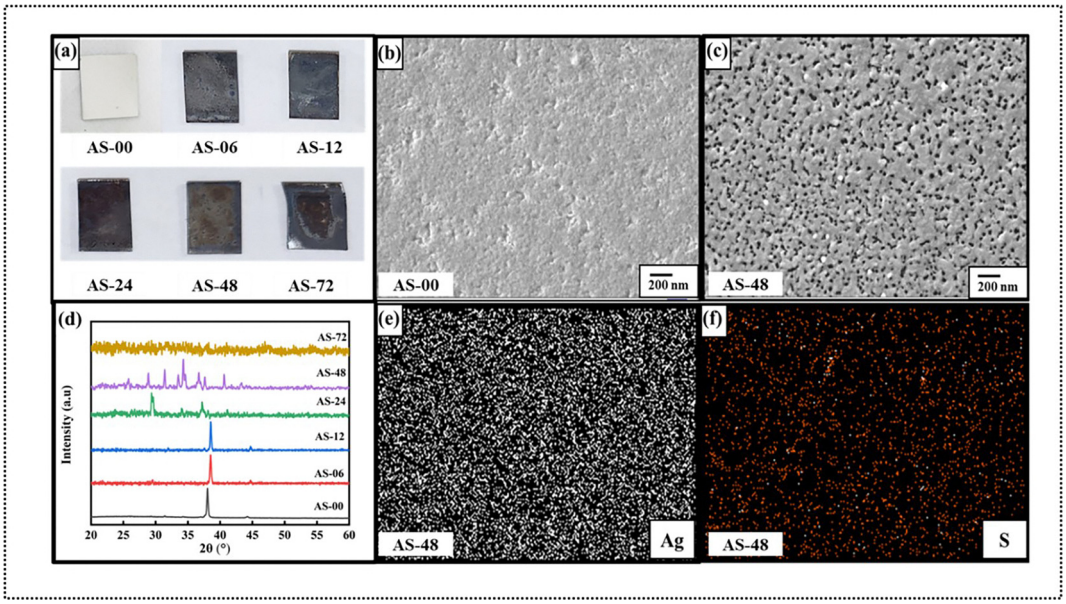

Fig. 1 (a) Visual inspection of Ag films after sulfurization for 6, 12, 24, 48, and 72 hours, along with the untreated Ag reference. (b) SEM image of pristine Ag film. (c) SEM image of the Ag_2S film after 48 hours of sulfurization. (d) XRD patterns of Ag films (AS-00 to AS-72) corresponding to different sulfurization durations. (e) and (f) EDS elemental mapping of the 48-hour Ag_2S film showing the distribution of (e) Ag and (f) S.

 © 2026 The Author(s). Published by the Royal Society of Chemistry

Open Access Article. Published on 20 January 2026. Downloaded on 1/20/2026 10:35:29 PM.
This article is licensed under a Creative Commons Attribution-NonCommercial 3.0 Unported Licence.

Table 1 XRD peak positions (2θ) and corresponding (*hkl*) planes of Ag and Ag_2S phases for samples AS-00 to AS-72

	AS-00	AS-06	AS-12	AS-24	AS-48	AS-72
Ag 2θ (°)	38.04 (100) 44.20 (200)	38.50 (100) 44.72 (200)	38.52 (100) 44.78 (200)	38.10 (100)		—
Ag_2S 2θ (°)	—	29.56 (111)	37.56 (−103)	29.38 (021) 29.56 (111) 34.00 (022) 37.20 (121) 41.14 (031)	31.40 (−112) 33.52 (111) 34.30 (022) 34.60 (022) 36.70 (013) 37.56 (−103) 40.62 (031) 43.30 (200)	—

exhibited reproducible unipolar RS behavior, as shown in Fig. 2a. The forming process required an initial high voltage sweep around 60 V, with the first switching event occurring at 48.7 V, indicated by a sharp current jump from 3.57 μA to the compliance limit of 10 μA. With successive cycles (Fig. S3), the set voltage decreased and stabilized in the range of 4.5–5.5 V for both 10 μA and 100 μA compliance (Fig. 2b and c), suggesting filament conditioning and lowered formation barriers. The reset transitions occurred consistently between 0.1 and 1 V, without polarity reversal, confirming a unipolar switching mechanism driven by Joule heating-induced filament dissolution. The current jump also changed from 0.023 μA to 10 μA (memory window 434) and 0.064 μA to 100 μA (memory window 1562.5), respectively, for 10 μA and 100 μA compliance. Similar behaviour has been widely reported in ECM-based Ag devices and is attributed to field-driven ion transport and thermally triggered rupture of metallic filaments.[41,42]

Endurance tests were conducted at two compliance current levels. At 10 μA, the device sustained stable switching over 100 cycles, whereas at 100 μA, stable operation was maintained for

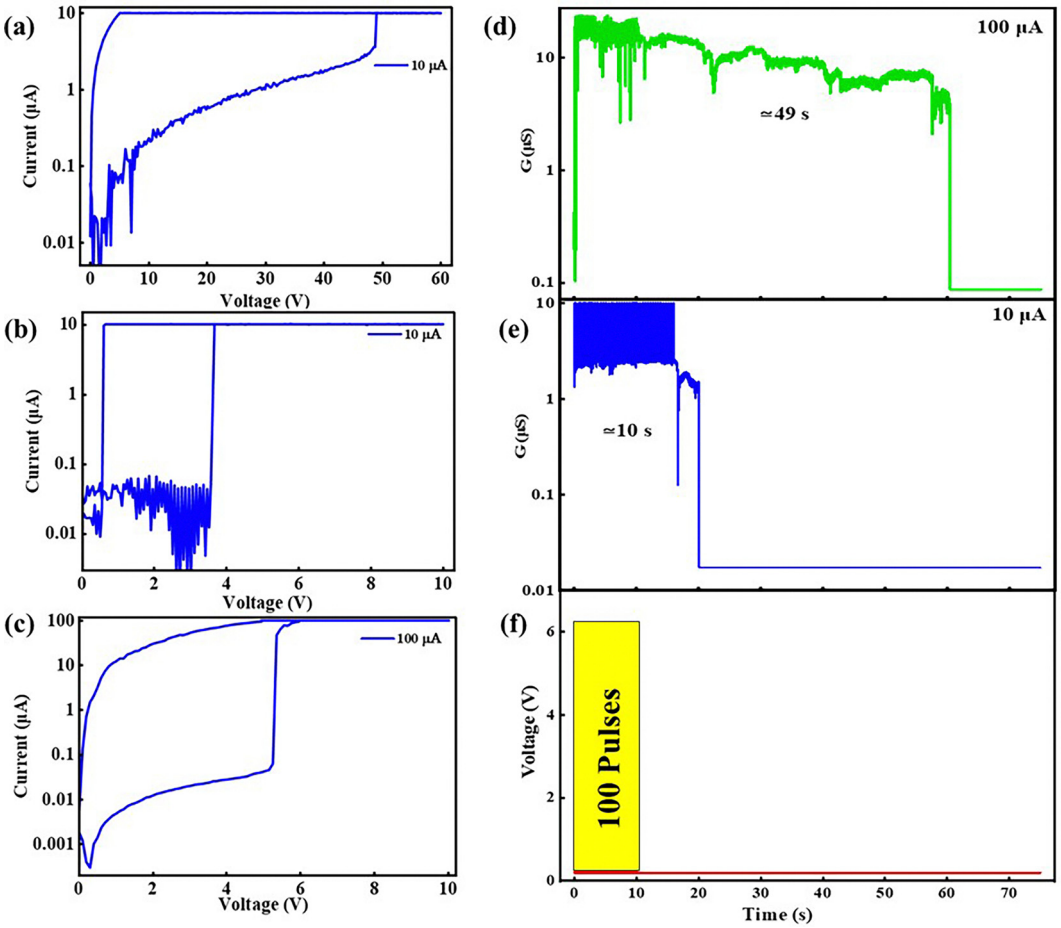

Fig. 2 (a) 1st RS cycle at 10 μA, RS graph at (b) 10 μA and (c) 100 μA. (d–f) Conductance potentiation and decay under 100 μA (green) and 10 μA (blue) current limits following pulsed stimulation.

Open Access Article. Published on 20 January 2026. Downloaded on 1/20/2026 10:35:29 PM.
This article is licensed under a Creative Commons Attribution-NonCommercial 3.0 Unported Licence.

25 cycles (Fig. S1a and b). The memory window, defined by the resistance ratio between the high-resistance state (HRS) and the low-resistance state (LRS), increased from 1.75×10^2 at 10 μA to 2.34×10^3 at 100 μA. This level of variability falls within the range typically reported for Ag_2S and other chalcogenide-based ECM systems.[26,43,44] The resistive switching and conductive characteristics of the Ag/Ag_2S/Ag devices prepared with different reaction times (AS 06, AS 12, AS 24, and AS 72) are provided in the supplementary information (Fig. S4 and S5). Samples AS 06–AS 24 show linear switching behavior, whereas AS 72 shows negligible conductivity. In comparison, AS 48 exhibits clear resistive switching behavior, indicating that a 48 hour reaction time is appropriate for device operation.

Device-to-device variability was rigorously evaluated across 20 fabricated devices, with 16 exhibiting successful and reproducible switching behavior. Statistical distributions from these functional devices reveal a forming voltage of 60 ± 15 V (Fig. 3a), SET voltage of 5 ± 2 V (Fig. 3b), RESET voltage of 1 ± 0.5 V (Fig. 3c), LRS resistance of 0.1 ± 0.05 MΩ (Fig. 3d), and HRS resistance of 0.2 ± 0.05 GΩ (Fig. 3e), yielding a robust memory window of $\sim 10^3$ (Fig. 3f). Notably, all 16 devices demonstrate consistent short-term plasticity emulation (Fig. 3g).

In pristine Ag_2S planar devices, the stoichiometric Ag_2S layer exhibits high resistivity without pre-existing conductive paths, necessitating a substantial electroforming voltage (~60 V, equivalent to ~0.55 MV cm^{-1}) across the 110 μm electrode

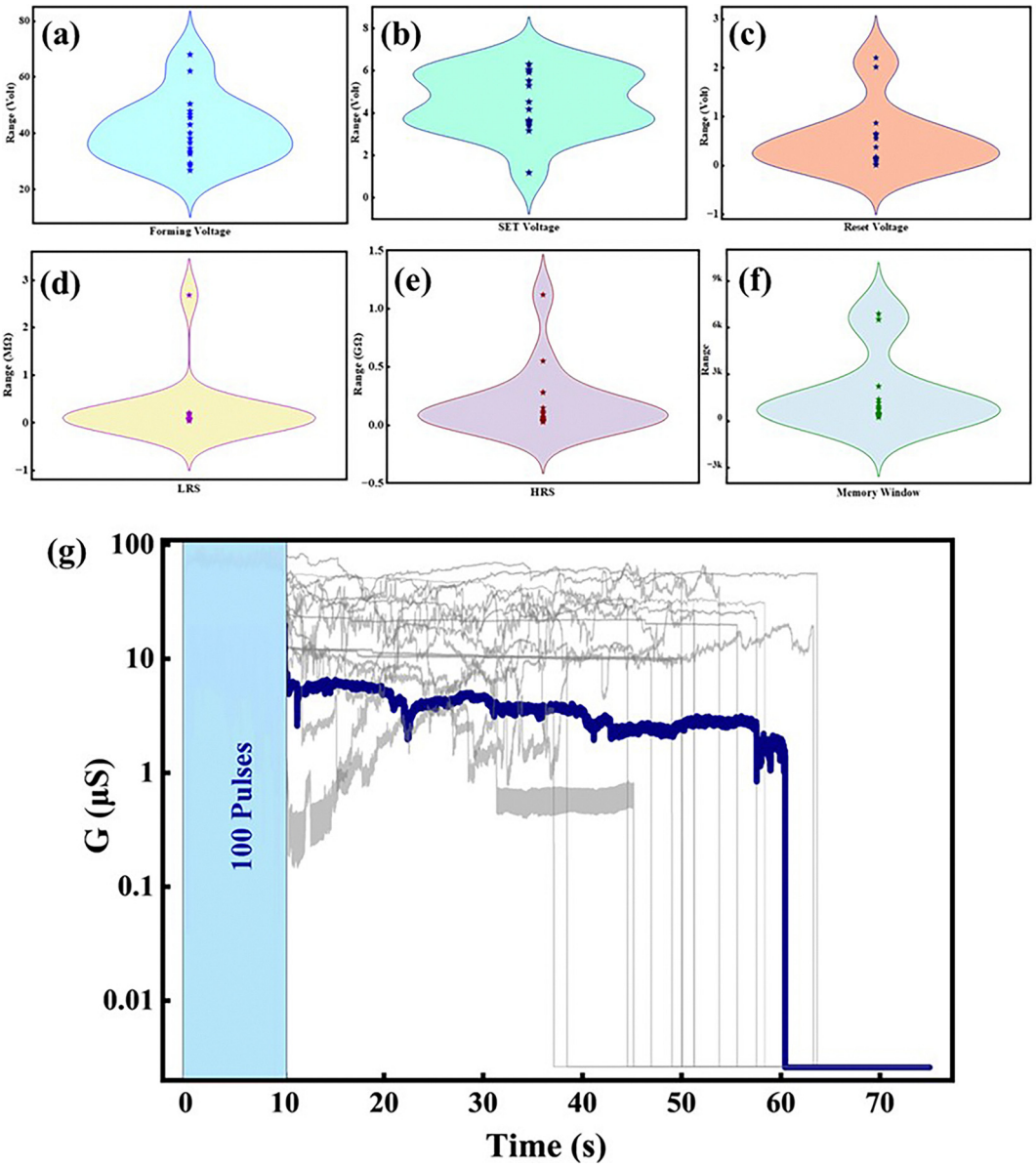

Fig. 3 Statistical distribution and synaptic conductance characteristics of the resistive switching devices. (a–f) Violin plots showing device-to-device variation (16 devices) of the key switching parameters: (a) forming voltage, (b) set voltage, (c) reset voltage, (d) low-resistance state (LRS) resistance, (e) high-resistance state (HRS) resistance, and (f) memory window. (g) Conductance (G) as a function of time under consecutive pulse stimulation, demonstrating short-term synaptic plasticity (STP) like conductance dynamics.

 © 2026 The Author(s). Published by the Royal Society of Chemistry

Open Access Article. Published on 20 January 2026. Downloaded on 1/20/2026 10:35:29 PM.
This article is licensed under a Creative Commons Attribution-NonCommercial 3.0 Unported Licence.

gap imposed by shadow mask limitations. This voltage drives Ag oxidation at the anode, Ag^+ ion migration, local supersaturation, nucleation, and dendritic filament formation to establish the conductive pathway.[45] Scaling down the electrode gap is anticipated to significantly lower the forming voltage, enhancing device scalability and practicality for neuromorphic applications. The RS mechanism is based on the electrochemical metallization process. Upon positive bias, Ag atoms at the active electrode oxidize ($Ag \rightarrow Ag^+ + e^-$), releasing Ag^+ ions into the Ag_2S matrix. These ions migrate under the electric field and are reduced ($Ag^+ + e^- \rightarrow Ag^0$) near the counter electrode, initiating filament nucleation. During the RESET process, local Joule heating dissolves the filament, thereby returning the device to HRS. The dynamic balance between filament formation and rupture underpins the observed RS behavior (Scheme S1a). The involvement of filament instability, especially under low to moderate compliance, has been mechanistically verified using kinetic models and thermal energy competition between filament surface and volume terms. Although a higher compliance current injected more Ag ions, the resulting filament structure remained volatile (Scheme S1b). This behavior is consistent with observations reported by La Barbera *et al.*,[20] who demonstrated that increased current compliance may lead to denser dendritic branching rather than thicker filaments. Their findings suggest that filament shape, particularly the density and connectivity of dendritic branches, can influence synaptic retention properties. Even at high current compliance, filaments composed of thin, branched structures tend to dissolve rapidly, maintaining STP characteristics. In this case study, the persistence of volatile switching and limited retention extension strongly suggests a similar morphology. Although direct imaging was not performed, the retention dynamics and electrical behaviour correlate well with this model. Such filament morphology governed by electrical history and current compliance can be tailored to emulate transient synaptic functions in neuromorphic systems.[20,46]

The device exhibited compliance, current-tunable switching, and retention behaviour, with well-defined ON/OFF ratios, endurance stability, and synaptic-like short-term memory. The ability to mimic biologically relevant plasticity through purely electrical control makes this planar Ag_2S platform a promising candidate for future low-power, short-term memory modules in neuromorphic architectures.

4 Conclusions

This study demonstrates a scalable, room-temperature strategy for synthesizing phase-pure α-Ag_2S films *via* controlled H_2S sulfidation of thermally deposited silver. Structural analysis confirms the complete transformation of FCC Ag to monoclinic Ag_2S within 48 hours, eliminating the need for high-temperature or vacuum-based processing. Planar Ag/Ag_2S/Ag memristors fabricated using this method exhibit highly reproducible unipolar resistive switching with excellent device-to-device uniformity, as evidenced by statistical distributions of forming voltage, SET/RESET voltages, HRS/LRS resistance levels, and memory window from 16 out of 20 devices.

The devices display robust STP governed by an electrochemical metallization mechanism, characterized by volatile conductance retention averaging ∼49 s at 100 μA compliance and high-to-low resistance ratios exceeding 10^3. This current-tunable volatility closely emulates the temporal dynamics of biological synapses, validating the material's potential for dynamic signal processing tasks. By combining a low-cost, ambient synthesis route with reliable synaptic functionality, this work establishes α-Ag_2S as a practical and accessible electrolyte for energy-efficient, neuromorphic short-term memory applications.

Author contributions

Shreepooja Bhat: conceptualization, data curation, formal analysis, investigation, methodology, project administration, validation, visualization, writing – original draft, writing – review & editing. Namitha Bannur: data curation, formal analysis, investigation, writing – original draft, writing – review & editing. Nanditha Thayyath Kizhakkeveettil: data curation, formal analysis, investigation, methodology, writing – original draft, writing – review & editing. Rajashekhar Pujar: data curation, investigation, validation, writing – review & editing. Gurumurthy Sangam Chandrasekhar (corresponding author): conceptualization, formal analysis, investigation, project administration, supervision, validation, visualization, writing – review & editing.

Conflicts of interest

The authors declare that they have no known competing financial interests or personal relationships that could have appeared to influence the work reported in this paper.

Data availability

Data will be made available on request.

Supplementary information (SI) is available. See DOI: https://doi.org/10.1039/d5ma01446h.

Acknowledgements

The authors are greatly indebted to their respective organisations. Shreepooja Bhat, Nanditha Thayyath Kizhakkeveettil, Namitha Bannur, Rajashekar Pujar and Gurumurthy Sangam Chandrasekhar acknowledge Manipal Institute of Technology, Manipal Academy of Higher Education, Manipal, for providing fellowship and facilities. The authors express their sincere gratitude to Dr Bharath B from the Manipal Institute of Applied Physics, Manipal, for his invaluable validation and insightful suggestions. During the preparation of this work, the authors used ChatGPT to improve language and readability. The authors reviewed and edited the content and take full responsibility for the publication's content. The use of ChatGPT was

Open Access Article. Published on 20 January 2026. Downloaded on 1/20/2026 10:35:29 PM.
This article is licensed under a Creative Commons Attribution-NonCommercial 3.0 Unported Licence.

limited to language enhancement and did not influence the scientific content, data interpretation, or conclusions.

References

1 Y. Xiao, C. Gao, J. Jin, W. Sun, B. Wang, Y. Bao, C. Liu, W. Huang, H. Zeng and Y. Yu, *Adv. Dev. Instrum.*, 2024, **5**, 0044.
2 S. J. Kim, S. B. Kim and H. W. Jang, *iScience*, 2020, **24**, 101889.
3 Y. Zhu, J. S. Liang, X. Shi and Z. Zhang, *ACS Appl. Mater. Interfaces*, 2022, **14**, 43482–43489.
4 O. Srikimkaew, S. Azhari, D. Banerjee, Y. Usami, H. Tanaka, O. Srikimkaew, D. Banerjee, Y. Usami, H. Tanaka and S. Azhari, *Adv. Electron. Mater.*, 2024, **10**, 2400360.
5 H. Kim, S. J. Yang, Y. S. Shim and C. W. Moon, *ACS Appl. Mater. Interfaces*, 2025, **17**, 50122–50141.
6 M. A. Shakib, Z. Gao and C. Lamuta, *ACS Appl. Electron. Mater.*, 2023, **5**, 4875–4884.
7 C. Li, X. Zhang, P. Chen, K. Zhou, J. Yu, G. Wu, D. Xiang, H. Jiang, M. Wang and Q. Liu, *iScience*, 2023, **26**, 106315.
8 E. Lee, J. Kim, S. Bhoyate, K. Cho and W. Choi, *Chem. Mater.*, 2020, **32**, 10447–10455.
9 R. A. Wells and A. W. Robertson, *Adv. Electron. Mater.*, 2024, **10**, 2400121.
10 F. Ghafoor, H. Kim, B. Ghafoor, M. A. Hamayun, M. F. Maqsood, M.-J. Lee and D. Kim, *Appl. Mater. Today*, 2025, **47**, 102959.
11 A. S. Sarkar, *Front. Electron.*, 2025, **6**, 1651937.
12 G. Li and Y. Lu, *J. Alloys Compd.*, 2025, **1020**, 179415.
13 R. Berdan, T. Prodromakis, A. Khiat, I. Salaoru, C. Toumazou, F. Perez-Diaz and E. Vasilaki, *Proc. IEEE Int. Symp. Circuits Syst.*, 2013, 425–428.
14 S. Ricci, D. Kappel, C. Tetzlaff, D. Ielmini and E. Covi, *Neuromorphic Comput. Eng.*, 2023, **3**, 044004.
15 X. Liang, Y. Zhong, X. Li, H. Huang, T. Li, J. Tang, B. Gao, H. Qian, H. Wu and H. Heidari, *ICECS 2022 - 29th IEEE International Conference on Electronics, Circuits and Systems, Proceedings*, DOI: 10.1109/ICECS202256217.2022.9970880.
16 Y. Ho Jang, J.-K. Han, S. Cheol, C. Hwang, H. Seong and Y. H. Jang, *InfoScience*, 2024, **1**, e12013.
17 C. Li, F. Zhu, X. Zhang, P. Chen, Y. Zhang, Y. Yang, L. Cheng, Y. Ding, M. Wang, Z. Yuan and Q. Liu, *IEEE Electron Device Lett.*, 2024, **45**, 284–287.
18 X. Wang, Y. Zhu, Z. Zhou, X. Chen, X. Jia, X. Wang, Y. Zhu, Z. Zhou, X. Chen and X. Jia, *Nanomaterials*, 2025, **15**, DOI: 10.3390/NANO15141130.
19 S. I. Sadovnikov and A. I. Gusev, *J. Mater. Chem. A*, 2017, **5**, 17676–17704.
20 S. La Barbera, D. Vuillaume and F. Alibart, *ACS Nano*, 2015, **9**, 941–949.
21 G. Li, Q. An, S. I. Morozov, B. Duan, W. A. Goddard, Q. Zhang, P. Zhai and G. J. Snyder, *NPJ Comput. Mater.*, 2018, **4**, 44.
22 X. Shi, H. Chen, F. Hao, R. Liu, T. Wang, P. Qiu, U. Burkhardt, Y. Grin and L. Chen, *Nat. Mater.*, 2018, **17**, 421–426.
23 S. I. Sadovnikov, M. G. Kostenko, A. I. Gusev and A. V. Lukoyanov, *Nanomaterials*, 2023, **13**, 2638.
24 B. Yang, Y. Zhang, M. He, Y. Duan, Z. Li and L. Yang, *J. Mater. Chem. C*, 2025, **13**(43), 21788–21796.
25 Y. Zhu, T. Nyberg, L. Nyholm, D. Primetzhofer, X. Shi and Z. Zhang, *Nanomicro Lett*, 2025, **17**, 1–12.
26 S. Jo, S. Cho, U. J. Yang, G. S. Hwang, S. Baek, S. H. Kim, S. H. Heo, J. Y. Kim, M. K. Choi and J. S. Son, *Adv. Mater.*, 2021, **33**, 2100066.
27 M. B. Baghirov, M. Muradov, G. Eyvazova, S. Mammadyarova, Y. Azizian-Kalandaragh, N. Musayeva, G. E. Kochari and R. F. Huseynali, *RSC Adv.*, 2024, **14**, 16696–16703.
28 M. B. Baghirov, M. Muradov, G. Eyvazova, Y. Azizian-Kalandaragh, S. Mammadyarova, J. Kim, E. Gasımov and F. Rzayev, *RSC Adv.*, 2024, **14**, 2320–2326.
29 P. Perrenot, S. Pairis, D. Bourgault and N. Caillault, *Vacuum*, 2019, **163**, 26–30.
30 A. I. Oje, A. A. Ogwu, M. Mirzaeian, A. M. Oje and N. Tsendzughul, *Appl. Surf. Sci.*, 2019, **488**, 142–150.
31 G. Cai, X. Zheng, Y. Zheng, Y. Xiao and Y. Zheng, *Mater. Lett.*, 2016, **178**, 248–251.
32 K. Raji, S. Thomas and C. B. Sobhan, *Appl. Surf. Sci.*, 2011, **257**, 10562–10570.
33 T. Blanton, S. Misture, N. Dontula and S. Zdzieszynski, *Powder Diffr.*, 2011, **26**, 114–118.
34 R. Bekkari, B. Jaber and L. Laânab, *J. Mater. Sci.: Mater. Electron.*, 2022, **33**, 12126–12136.
35 S. Soni, S. Kumar, B. Dalela, S. Kumar, P. A. Alvi and S. Dalela, *J. Alloys Compd.*, 2018, **752**, 520–531.
36 T. E. Graedel, *J. Electrochem. Soc.*, 1992, **139**, 1963–1970.
37 A. S. Baburin, A. I. Ivanov, E. S. Lotkov, O. S. Sorokina, I. A. Boginskaya, E. V. Sergeev, K. A. Buzaverov, T. G. Konstantinova, D. O. Moskalev, Z. Issabayeva, I. A. Ryzhikov and I. A. Rodionov, *Coatings*, 2020, **10**, 911.
38 E. Barrera-Calva, M. Ortega-López, A. Avila-García and Y. Matsumoto-Kwabara, *Thin Solid Films*, 2010, **518**, 1835–1838.
39 W. Dong, J. Fu, J. Yang, S. Ren, H. Zhu, Y. Wang, J. Hao, Y. Zhang and Z. Zheng, *J. Mater. Chem. C*, 2023, **11**, 16842–16858.
40 D. L. Douglass, *Sol. Energy Mater.*, 1984, **10**, 1–7.
41 E. L. Lee, Y. S. Goh, A. S. M. A. Haseeb, Y. H. Wong, M. F. M. Sabri and B. Y. Low, *J. Electrochem. Soc.*, 2023, **170**, 021505.
42 T. S. Lee, N. J. Lee, H. Abbas, H. H. Lee, T. S. Yoon and C. J. Kang, *ACS Appl. Electron. Mater.*, 2020, **2**, 1154–1161.
43 O. Srikimkaew, S. Ricci, M. Porzani, T. Tan Dang, Y. Nakaoka, Y. Usami, D. Ielmini, H. Tanaka, O. Srikimkaew, T. T. Dang, Y. Nakaoka, Y. Usami, H. Tanaka, S. Ricci, M. Porzani, D. Ielmini, P. L. da Vinci and I. Y. Usami, *Adv. Electron. Mater.*, 2024, **10**, 2300709.
44 Y. Li and K.-W. Ang, *Adv. Intell. Syst.*, 2021, **3**, 2000137.
45 W. Sohn, H. Kim, J. H. Lee, Y. S. Shim, C. W. Moon and H. Kim, *Mater. Adv.*, 2025, **6**, 4158–4173.
46 T. Ohno, T. Hasegawa, T. Tsuruoka, K. Terabe, J. K. Gimzewski and M. Aono, *Nat. Mater.*, 2011, **10**, 591–595.

 © 2026 The Author(s). Published by the Royal Society of Chemistry